Applied Physics B (2023) 129:25
https://doi.org/10.1007/s00340-022-07964-y

Applied Physics B
Lasers and Optics

RESEARCH

Time-resolved laser-induced incandescence on metal nanoparticles: effect of nanoparticle aggregation and sintering

S. Robinson-Enebeli[1] · S. Talebi-Moghaddam[1] · K. J. Daun[1]

Received: 19 August 2022 / Accepted: 22 December 2022 / Published online: 11 January 2023

Abstract
This work examines the excessive absorption and anomalous cooling phenomena reported in laser-induced incandescence measurements on metal nanoparticles by considering the effects of aggregate structure and sintering. Experimental investigations are conducted on iron and molybdenum aerosols, which have different melting points, and thus respond differently to the laser pulse. Although aggregation enhances the absorption cross-section of the nanoparticles and allows for higher peak temperatures, this enhancement does not fully explain the observed excessive absorption. Furthermore, as the aggregates of refractory metals such as molybdenum cool, they may sinter through gradual grain boundary diffusion; this change in structure alters their absorption cross-section, manifesting as a rapid drop in the pyrometric temperature, which could explain the anomalous cooling reported for this metal.

1 Introduction

Metal nanoparticles are increasingly applied in a wide range of fields. For example, zero-valent iron nanoparticles combined with oxidants are used to treat water by removing heavy metal contaminants through adsorption [1]; noble metal nanoparticles are used for hyperthermia cancer therapy due to their ability to convert EM waves into heat [2, 3]; and some metal nanoparticles are used as nodes in metal–organic frameworks to encapsulate and deliver drugs to targeted bio locations [4]. Since the various applications of metal nanoparticles depend on their properties, which, in turn, are strong functions of particle morphology, there is a need for optical diagnostics that can characterize the size, shape, and concentrations of metal nanoparticles in the gas phase.

Time-resolved laser-induced incandescence (TiRe-LII), a laser diagnostic normally used to interrogate soot-laden aerosols [5–7], is increasingly applied to examine metallic aerosols [8, 9]. The technique involves heating aerosolized nanoparticles to incandescent temperatures with a laser pulse, after which time the nanoparticles return to thermal equilibrium with the bath gas. During this process, radiative emissions from the aerosol are collected at several wavelengths and may be used to infer various aerosol attributes, including the particle size distribution and volume fraction, using a measurement model. The model consists of a spectroscopic sub-model that relates the nanoparticle emissions to their temperature and volume fraction, and a heat transfer sub-model that relates the observed temperature decay to their size distribution. While particle size and volume fraction are usually the focus of soot-based measurements, TiRe-LII measurements on metal aerosols have also been used to infer the thermal accommodation coefficient (TAC) [10–12], heat capacity [13], radiative properties [14], and composition of the nanoparticles [15].

Although this technique is highly promising, there remain some anomalies in the data that cannot be explained with current measurement models (cf. Fig. 1) [8, 9, 16]. One such anomaly is excessive absorption, in which the peak experimental temperatures reached by laser-heated nanoparticles exceed those that are theoretically predicted based on the absorption cross-section of the particles determined through electromagnetic theory [8, 9]. Another anomaly is so-called anomalous cooling, whereby the observed pyrometric temperature decays at a much greater rate immediately after the peak temperature than can be explained by current cooling models [8, 9].

Several hypotheses have been proposed to explain these phenomena. Talebi-Moghaddam et al. [16] explained

✉ S. Robinson-Enebeli
stephen.robinson-enebeli@uwaterloo.ca

[1] Department of Mechanical and Mechatronics Engineering, University of Waterloo, 200 University Ave. West, Waterloo, ON N2L 3G1, Canada

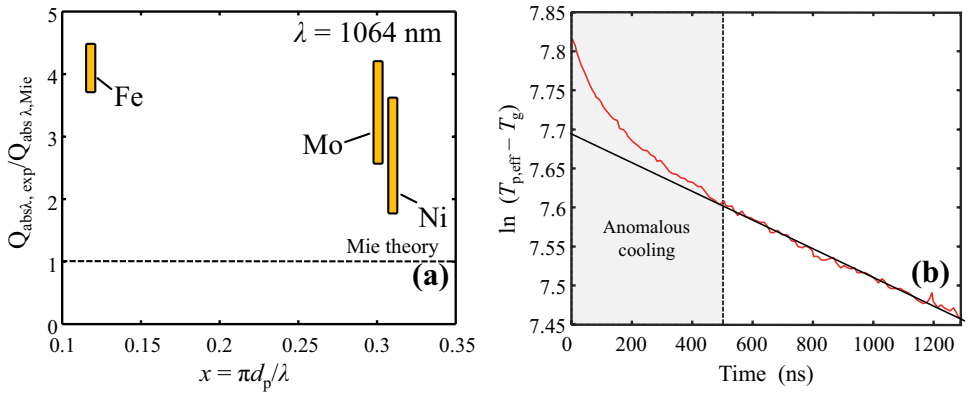

Fig. 1 **a** Excessive absorption phenomenon exhibited by Fe and Mo (computed from this work assuming isolated primary particles) and Ni [8] and **b** anomalous cooling phenomenon adapted from Ref. [9]; the experimental pyrometric temperature (red curve) drops more rapidly than the expected linear conduction curve (black curve) within the first ~ 500 ns following the peak temperature. $Q_{abs\lambda,exp}$ and $Q_{abs\lambda,Mie}$ are the absorption efficiency determined from experiments and computed from Mie theory, respectively, for a primary particle with diameter of d_p at an excitation wavelength λ. $T_{p,eff}$ is the effective aerosol temperature and T_g is the temperature of the bath gas

the apparent excessive absorption of noble metals by observing that the measured LII signal, under 1064 nm irradiation, does not originate from incandescence, but rather from multiphoton-induced photoluminescence. For other metals, the pyrometrically inferred peak temperature may be inflated due to corruption of the LII signals by broadband inverse neutral Bremsstrahlung, which could happen at fluences above 10 mJ/mm^2 [17]. Talebi-Moghaddam et al. [18] also showed that some reports of excessive absorption in the literature could be attributed, in part, to improper use of the Rayleigh approximation of Mie theory to model the absorption cross-sections of metal nanoparticles at the excitation wavelength. Eremin et al. [14] observed apparent enhanced absorption cross-sections in metal aerosols produced by photolysis of $Fe(CO)_5$ using an excimer laser, followed by a second LII laser pulse. They suggest that this effect may depend, in some way, on the particle diameter, which was controlled by changing the delay between the excimer laser pulse and the LII pulse.

In contrast to the enhanced absorption phenomenon, which is more pronounced for metal nanoparticles, anomalous cooling has been observed in LII measurements on both carbonaceous [19, 20] and metal [8, 9, 21] aerosols, although it is unclear whether these observations may be attributed to the same underlying cause. Both Gurentsov et al. [21] and Sipkens et al. [9] report a rapid temperature decrease of Mo nanoparticles following the peak temperature. If neutral Bremsstrahlung occurs, Talebi-Moghaddam et al. [17] also speculate that the anomalous cooling effect could be due to the gradual dissipation of a laser-induced plasma surrounding the particle, leading to a corresponding decay in the signal corruption and drop in pyrometric temperature. Altman [22] has additionally speculated that the prolonged electron relaxation could explain the anomalous cooling phenomenon.

In all LII studies on metal nanoparticles discussed hitherto, aerosolized nanoparticles are assumed to exist as isolated spheres and are modeled as such, while in reality, the particles are often nanospheres arranged in an aggregate structure. This conceptual simplification is mostly benign for soot, since, according to Rayleigh–Debye–Gans Fractal Aggregate (RDG-FA) theory [23], the absorption cross-section of the aggregate is approximated by the sum of the absorption cross-sections of the primary particles (multiple scattering within the aggregate is neglected). However, RDG-FA theory does not generally apply to aggregates of metal nanospheres [18]. Moreover, the aggregate structure may change significantly due to laser-induced changes in morphology that will result in a change in the spectral absorption cross-section during excitation and cooling, consequently biasing the pyrometrically inferred temperatures.

This paper describes TiRe-LII measurements carried out on aerosols of iron nanoparticles generated using a spark discharge generator and molybdenum aerosols produced by atomizing a commercial powder dispersed in water. Results from laser-heated Fe nanoparticles showed that accounting for aggregation reduces the magnitude of excessive absorption but does not completely eliminate this phenomenon. Measurements on Mo nanoparticles reveal that anomalous cooling is independent of the bath gas, which disallows the possibility that this effect is due to Bremsstrahlung contamination of the signal. Instead, simulations on laser-heated Mo nanoparticles suggest that grain boundary sintering of the nanoaggregate during laser heating changes the absorption properties of the

nanoaerosol, which manifests as an anomalous cooling immediately after the peak pyrometric temperature.

2 Theoretical modeling

Almost all previous LII studies on metal nanoparticles treat the particles as isolated spheres. However, many metal aerosols consist of aggregates of nanospheres. Furthermore, the number of primary particles per aggregate, N_p, or, equivalently, the radius of gyration, R_g, usually obeys a wide distribution due to the random processes underlying aggregate assembly [24]. These parameters are usually empirically related by $Np = kf(2Rg/dp)^{Df}$, where D_f and k_f are fractal dimension and pre-factor, respectively, which together define the aggregate morphology; D_f is a strong metric that defines the openness and compactness of the aggregates (a higher value of D_f represents more compact aggregates).

Accordingly, we consider three scenarios: (1) the aerosol may consist of isolated spheres of non-uniform diameter; (2) it may consist of non-uniformly sized aggregates containing uniformly sized primary particles; and (3) the aggregates may partially sinter upon laser heating into a different morphology, and, in a limiting case, into an aerosol of non-uniformly sized spheres.

In the case of an aerosol of metal aggregates, during an LII measurement, the temperature of an aggregate containing N_p nanoparticles with no overlap or necking, T_{agg}, is governed by [25, 26]

$$\begin{aligned}\frac{\pi}{6}d_p^3 N_p \rho_m c_m \frac{dT_{agg}}{dt} =& q_{laser,agg}(t, d_p, N_p) \\ &- q_{evap,agg}\left[T_{agg}\left(d_p, N_p\right)\right] \\ &- q_{cond,agg}\left[T_{agg}\left(d_p, N_p\right)\right]\end{aligned} \tag{1}$$

where ρ_m and c_m are the density and specific heat of the bulk nanoparticle material, respectively, d_p is the diameter of the primary particles within the aggregate, $q_{evap,agg}$ and $q_{cond,agg}$ are the evaporation and conduction heat transfer losses of the aggregate, respectively, and $q_{laser,agg}$ is the amount of laser heat absorbed by the aggregate. The model assumes that the aggregates are made of uniform primary particles; hence, temperature non-uniformities within the aggregate, as a consequence of polydisperse primary particle sizes, are negligible. (Non-uniform heating of the aggregate due to local field enhancements is not considered in this study, but should be considered in future work). Experimental primary particle distributions shown in later sections are observed to be sufficiently narrow to validate this assumption. In addition, the small Biot number calculated for Ni nanoparticles [8] during laser irradiation further suggests isothermality within the aggregate during heating. Radiation heat loss is negligible at commonly encountered temperatures (below 3500 K) [9].

The rate of mass loss from the aggregate is due to uniform evaporation from each particle within the aggregate and is given by [26]

$$\frac{dm_p}{dt} = -M_v \frac{q_{evap,agg}\left[T_{agg}\left(d_p, N_p\right)\right]}{\Delta H_v N_p} \tag{2}$$

where m_p is the mass of the nanoparticle, and M_v and ΔH_v are the molar mass and latent heat of evaporation of the bulk nanoparticle material, respectively; ΔH_v is computed by Watson's equation [27]. The diameter of each primary particle is assumed to change over time due to mass loss from evaporation and a decrease in density due to thermal expansion. The instantaneous primary particle diameter can be found from

$$d_p\left(T_p, m_p\right) = \left[\frac{6m_p}{\pi \rho_m(T_{agg})}\right]^{1/3} \tag{3}$$

and the instantaneous equivalent volumetric diameter of the aggregate can be computed from $d_v = d_p\,(T_p, m_p)\cdot(N_p)^{1/3}$.

The heat gain term $q_{laser,agg}$ is modeled according to

$$q_{laser,agg}(t, d_p) = F_0 f(t) C_{abs,\lambda}\left(\boldsymbol{m}_\lambda, d_p, N_p, k_f, D_f\right) \tag{4}$$

where F_0 is the laser fluence, $f(t)$ is the temporal laser profile, and $C_{abs,\lambda}(m_\lambda, d_p, N_p, k_f, D_f)$ is the absorption cross-section of the target. The absorption cross-section for an isolated nanosphere is $C_{abs,\lambda} = Q_{abs,\lambda}(m_\lambda, d_p)\cdot(\pi d_p^2/4)$ where $Q_{abs,\lambda}(m_\lambda, d_p)$ is the absorption efficiency computed from Mie theory with a refractive index of m_λ. In the case of aggregates, $C_{abs,\lambda} = Q_{agg,abs,\lambda}(m_\lambda, d_p, N_p, k_f, D_f)\cdot(\pi d_v^2/4)$, where $Q_{agg,abs,\lambda}$ is the absorption efficiency of the aggregate, assumed to consist of spheres in point contact, and $d_v = d_p\cdot(N_p)^{1/3}$ is the volumetric equivalent diameter of the aggregate. $Q_{agg,abs,\lambda}$ is computed from the multi-sphere T-matrix (MSTM) method [9, 10] for a randomly oriented aggregate at the laser wavelength, λ, and defined with respect to the equivalent diameter of the aggregate.

Equations (1) and (2) are solved simultaneously starting from an initial temperature taken to be that of the bath gas. Details about the evaporative and conductive cooling terms in Eq. (1) are provided in the Supplementary Information. These equations also apply to aerosols consisting of isolated nanospheres.

For aerosols containing aggregates, the number of primary particles per aggregate is defined by a probability density function (PDF), $p(N_p)$ and the measured incandescence is given by

$$J_\lambda(t) = C_\lambda \Lambda \int_0^\infty p(N_p) C_{abs,\lambda}(m_\lambda, d_p, N_p, k_f, D_f) I_{\lambda,b}[T_{agg}(t, N_p, d_p)] dN_p \tag{5}$$

where C_λ is the calibration constant, Λ is the intensity scaling factor (ISF) that accounts for the volume fraction of nanoparticles [28, 29], and $I_{\lambda,b}$ is the blackbody spectral intensity at the aggregate temperature, $T_{agg}(t,N_p,d_p)$. In some cases, it is convenient to envision the aerosol as consisting of aggregates having uniform d_p and N_p. In this scenario, Eq. (5) simplifies to

$$J_\lambda(t) = C_\lambda \Lambda C_{abs,\lambda}(m_\lambda, d_p, N_p, k_f, D_f) I_{b,\lambda}[T_{agg}(t, N_p, d_p)] \tag{6}$$

Equation (5) can also be used to model emitted incandescence from an aerosol containing isolated spheres where the PDF defines the distribution of the sphere diameters, and the absorption efficiency can be computed from Mie theory.

The experimental incandescence signals measured at any two detection wavelengths can be used to find an "effective" temperature, T_{eff}, of the nanoparticle ensemble

$$T_{p,eff} = \frac{hc_0}{k_B}\left(\frac{1}{\lambda_2} - \frac{1}{\lambda_1}\right) \left[\ln\left(\frac{J_{\lambda,1}}{J_{\lambda,2}} \frac{C^{eff}_{abs,\lambda 2}(m_\lambda, d_p, N_p, k_f, D_f)}{C^{eff}_{abs,\lambda 1}(m_\lambda, d_p, N_p, k_f, D_f)} \left(\frac{\lambda_1}{\lambda_2}\right)^5\right)\right]^{-1} \tag{7}$$

where h, c_0, and k_B are Planck's constant, the speed of light, and Boltzmann constant, respectively, and $C^{eff}_{abs,\lambda}$ is the effective absorption cross-section of the aerosol that considers all size classes. When considering spheres that emit radiation in the Rayleigh regime, where the phase function, $|m_\lambda|\pi d_p/\lambda << 1$, and size parameter, $\pi d_p/\lambda << 1$ [23, 30, 31], $Q_{abs,\lambda} = 4(\pi d_p/\lambda)E(m_\lambda)$, where $E(m_\lambda)$ is the spectral absorption function given by

$$E(\mathbf{m}_\lambda) = \mathrm{Im}\left(\frac{\mathbf{m}_\lambda^2 - 1}{\mathbf{m}_\lambda^2 + 2}\right) \tag{8}$$

In this scenario, the pyrometric nanoparticle temperature simplifies to

$$T_{p,eff} = \frac{hc_0}{k_B}\left(\frac{1}{\lambda_2} - \frac{1}{\lambda_1}\right)\left[\ln\left(\frac{J_{\lambda,1}}{J_{\lambda,2}} \frac{E(\mathbf{m}_{\lambda,2})}{E(\mathbf{m}_{\lambda,1})} \left(\frac{\lambda_1}{\lambda_2}\right)^6\right)\right]^{-1}. \tag{9}$$

A thermodynamic average temperature of the nanoparticles within the aerosol can be calculated if the size distribution and temperatures of each size class within the aerosol are known accurately. For example, for an aerosol containing isolated, non-uniformly sized spheres

$$T_{p,thermo} = \frac{\int_0^\infty T(d_p) c_m(T_p) \rho_m(T_p) d_p^3 p(d_p) \mathbf{d} d_p}{\int_0^\infty c_m(T_p) \rho_m(T_p) d_p^3 p(d_p) \mathbf{d} d_p} \tag{10}$$

A similar equation may be written for an aerosol containing non-uniformly sized aggregates of identical spheres, by substituting $p(N_p)$ in place of $p(d_p)$.

An advantage of Eq. (9) is that the pyrometric temperatures do not rely on the nanoparticle morphology; thus, the spectroscopic and heat transfer models may be applied sequentially to recover the quantities-of-interest. However, since the Rayleigh approximation to Mie theory is usually invalid for the metal nanoparticle sizes studied using LII, the pyrometric temperature computed in this manner loses its physical significance [18]. Consequently, there is non-uniform heating of the aggregates within the aerosol since the absorption cross-section is no longer proportional to $N_p d_p^3$ (i.e., no volumetric heating of the aggregates as opposed to the case of soot where RDG-FA applies). Nevertheless, pyrometry provides a general indication of the instantaneous temperature of the nanoparticles within the probe volume and can be used as a tool to reduce the dimension of the available data when inferring nanoaerosol attributes using inverse analysis techniques [9, 18]. However, Fig. 2 shows the non-uniform temperatures within the aerosol and that the pyrometric temperature may not always agree with the average thermodynamic temperature of the nanoparticles within the aerosol.

2.1 Sintering models for aggregates

Metal aggregates at elevated temperatures may undergo grain boundary diffusion sintering or viscous sintering, depending on their melting points [32].

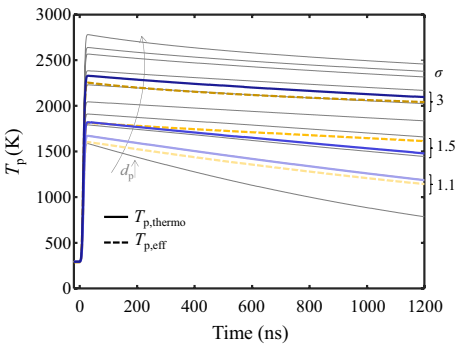

Fig. 2 Temperature evolutions showing the discrepancy, as a function of size distribution width, between the pyrometric temperature (dashed yellow curves) and the average thermodynamic temperatures (solid blue curves); gray curves show the temperatures of the different size classes within the aerosol. Simulations are performed with the properties of Fe nanoparticles irradiated at a fluence of 2.45 mJ/mm^2

When aggregates within the aerosol remain below their melting point, they sinter through grain boundary diffusion. For an identical two-sphere system, the evolution of the distance between the center of one of the spheres and the grain boundary, x, is given by [33]

$$x^5 dx = \frac{16 D_{gb}(T)\delta_{gb}\gamma_{sv}\Omega d_{p0}^2}{4k_B T} dt \tag{11}$$

where the grain boundary diffusivity for single crystals is

$$D_{gb} = D_0 \exp\left(-\frac{Q}{k_B T}\right) \tag{12}$$

and D_0 and Q are the pre-exponential factor and activation enthalpy, respectively, δ_{gb} is the grain boundary thickness which is the initial size of the monomer d_{p0} (at $x_0 = d_{p0}$), γ_{sv} is the surface energy, Ω is the atomic volume, and T is the temperature at the grain boundary. In this work, Eq. (11) is solved with the boundary condition of $x_0 = d_{p0}$. In this case, one would expect the laser pulse to temporally modify the aggregate structure, and hence its spectral absorption cross-section.

If the aggregates are heated to temperatures above their melting point, they sinter through viscous flow, which is much faster than grain boundary diffusion [33]. Viscous flow has a characteristic sintering time of [34]

$$\tau = \frac{\eta r_0}{\gamma}\left(\frac{N_p}{2}\right)^{(1/2 - D_f/6)} \tag{13}$$

where η and γ are the viscosity and surface tension of the material, respectively, and r_0 is the initial radius of the primary particles within the aggregate. The time scale for viscous sintering is below a nanosecond for the aggregates in this study, suggesting that particles heated beyond their melting point should, in principle, form nanospheres almost immediately.

Although there are other mechanisms of sintering [35], only grain boundary and viscous sintering are densifying mechanisms characterized by shrinkage as a consequence of particle centers approaching each other. Low-melting-point metals are expected to undergo viscous sintering at high temperatures since they become amorphous upon melting.

3 Experimental apparatus

This section describes the excitation and detection systems used to collect the experimental LII signals as well as the aerosol generation systems used to produce the synthesized metal nanoparticles.

3.1 Excitation and detection systems

TiRe-LII experiments were conducted using the apparatus shown in Fig. 3. The excitation system consists of a 1064 nm Nd:YAG laser operated at 20 Hz with a Gaussian pulse duration of 8 ns at FWHM. The laser pulse passes through beam-forming optics to control the power and cross-section of the final laser pulse contained within the probe volume.

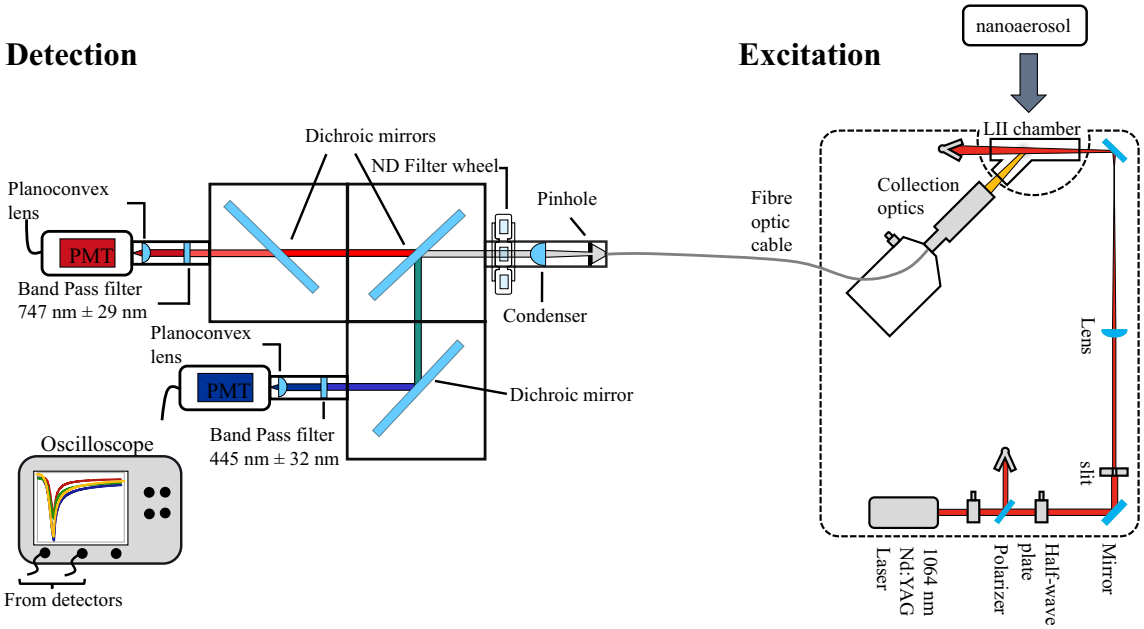

Fig. 3 Excitation and detection system used to conduct TiRe-LII experiments in this work

Additional details of the excitation system are provided in Ref. [8]. Emissions from the heated aerosol are focused onto a fiber optic cable using collection optics consisting of two achromatic doublets of focal lengths 210 and 100 mm. The fiber optic cable transmits emissions from the probe volume to the detection system consisting of a demultiplexing system which uses a series of dichroic mirrors and bandpass filters to decouple the light into two wavelength bands centered at 445, and 747 nm ± 29 nm, which are then imaged onto two PMTs. Signals were normalized to the 747 nm band using a tungsten–halogen light source (Thorlabs, SLS202L), with known emission spectra at 2800 K, following a calibration procedure similar to the one described in Ref. [36].

3.2 Aerosol generation

Aerosols of Fe and Mo aggregates are produced using the systems shown in Fig. 4. An aerosol of Fe nanoaggregates in N_2 (at a feed pressure of 1.2 bar) was generated using a spark discharge generator (SDG, PALAS GFG 1000, cf. Fig. 4) equipped with pure iron electrodes (ARMCO® – 99.85% iron) and operated at 270 Hz. In principle, it is possible to supply the SDG with various motive gasses, but the gas species affect the morphology of the nanoparticle [37]. Therefore, comparing LII signals collected from SDG-generated nanoparticles in different gasses is not straightforward. For this reason, the SDG is operated using N_2 exclusively.

TEM grids were populated with an electrostatic sampler (ESPNano – Model 100, 10 – 20 s sampling time). Size distribution analysis of 96 nanoparticles and 24 aggregates using ImageJ [38] showed that the primary particles within aggregates were lognormally distributed with ln$N$(6.02 nm, 1.3). The number of particles per aggregate was inferred to be ln$N$(126, 1.77) based on total surface area according to Ref. [39] assuming a projected area exponent of unity. Figure 5 highlights that the distribution of the number of particles per aggregate is larger than the primary particle size distribution suggesting that aggregate sizes within the aerosol mostly differ by N_p, which supports the approximation of uniform d_p underlying Eq. (5).

An attempt was made to produce spark discharge-generated Mo aerosols from molybdenum electrodes; however, the spark power generated by the PALAS generator was not sufficient to ablate the electrodes to produce a Mo aerosol with a high enough volume fraction to emit reliable LII signals; hence, a different route was explored. A colloidal solution of Mo nanopowder (MilliporeSigma) was aerosolized using a pneumatic atomizer (Model 3067 Constant Output Atomizer) with Ar, He, Ne, N_2, or CO_2 bath gasses, each supplied at a pressure of 20 psi. The wet aerosol flows through a diffusion dryer before entering the probe volume. The Mo aggregates showed varying degrees of compactness and openness; a representative TEM micrograph is shown in Fig. 4. Size distribution analysis of 125 nanoparticles showed the primary size distribution

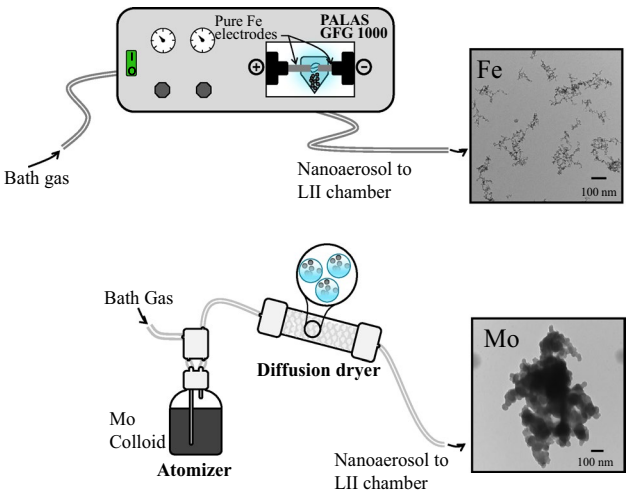

Fig. 4 Spark discharge generation and aerosolization system used in this work and the TEM micrographs of SDG-produced (at a spark frequency of 270 Hz) Fe and aerosolized Mo nanoaggregates

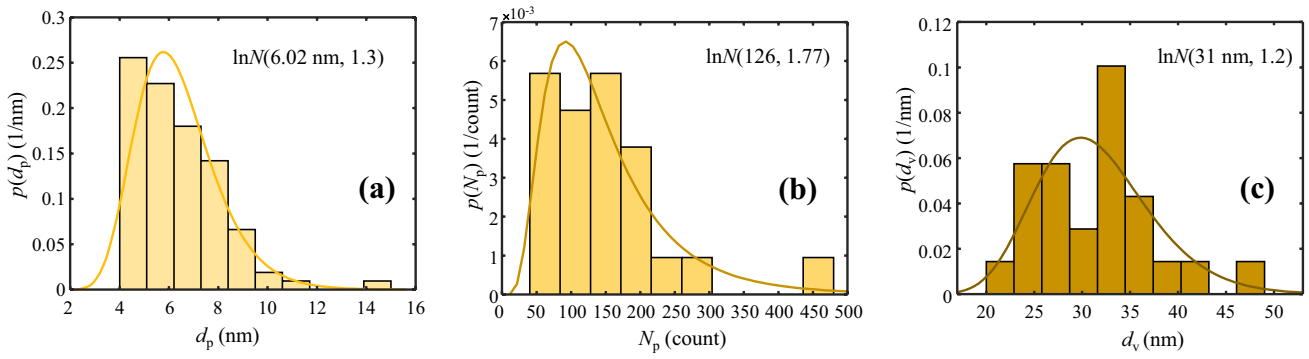

Fig. 5 The distribution of the **a** primary particle, **b** number of particles per aggregate, **c** equivalent diameter of the SDG-generated Fe aerosol. The equivalent diameter distribution is computed from the mean of the primary particle distribution

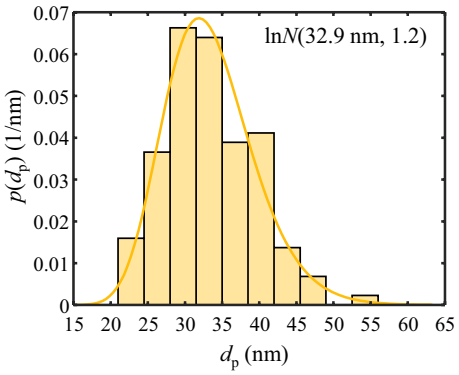

Fig. 6 Primary particle size distribution of the aerosolized Mo nanocolloid

lnN(32.9 nm, 1.2) (cf. Figure 6). The analysis of the number of particles per aggregate was inconclusive due to the low number of aggregates observed on the TEM micrographs which ranged from 40 to 200 particles per aggregate; hence, the sample size was not enough to determine a distribution.

To explore how the particles may respond to the laser pulse, another set of TEM-sampled nanoaggregates are prepared and directly irradiated with one laser shot with a fluence of 2.45 mJ/mm^2. It is experimentally challenging to image a particular set of particles on a TEM grid before and after irradiation due to uncertainties in grid placement and grid distortion from irradiation. As seen in Fig. 7a, the Fe aggregates sinter into isolated spheres that are much larger than the estimated volumetric diameter of the aggregates, cf. Fig. 5c. It is possible that several aggregates on the TEM grid may merge into a single large sphere. It should also be noted that during irradiation of TEM-sampled nanoaggregates, the TEM grids will act as heat sinks to remove heat from the particles causing particles to cool much faster compared to irradiation in an aerosol; consequently, particles may sinter differently on the grids than in aerosol form.

4 Results and discussion

4.1 Comparison of LII signals

Figures 8a, b show typical LII traces for the Fe and Mo aggregates in N_2 at a fluence of 2.45 mJ/mm^2. Signals are produced by averaging over 40 shots. Unless otherwise

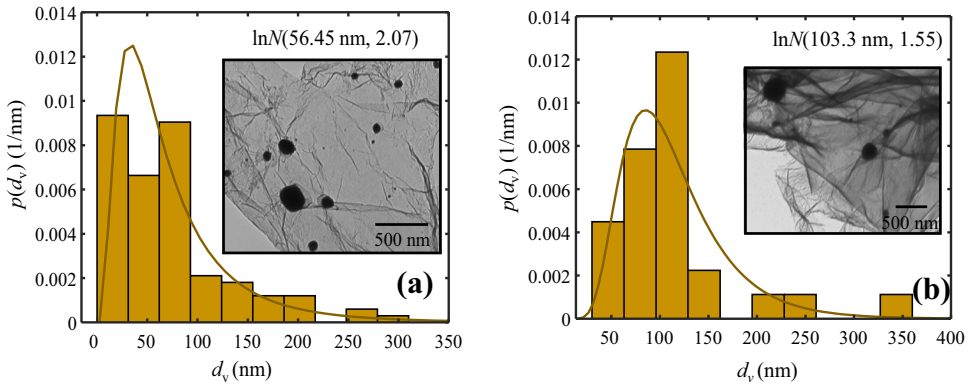

Fig. 7 TEM images and size distributions of **a** Fe and **b** Mo nanoparticles irradiated on the TEM grid

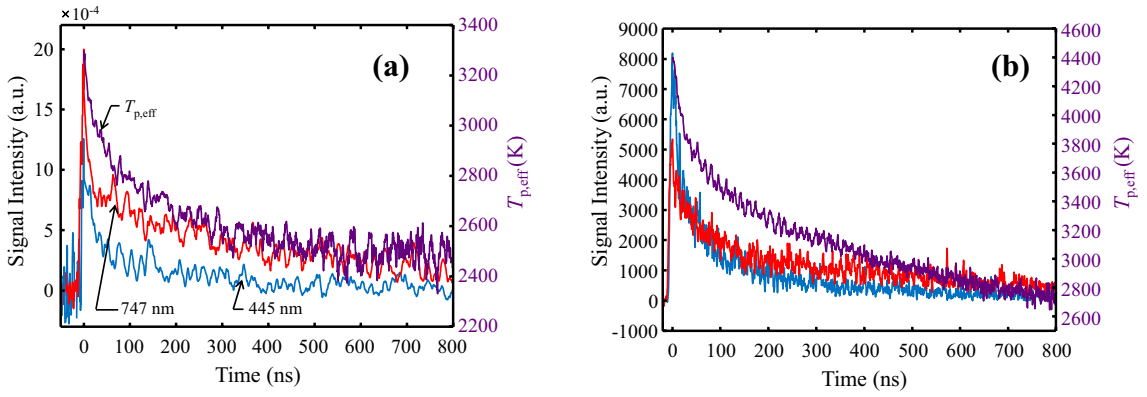

Fig. 8 Sample LII traces and pyrometric temperatures for **a** Fe nanoparticles in N_2; and **b** Mo nanoparticles in Ar, irradiated at a fluence of 2.45 mJ/mm^2

Table 1 Refractive indices of Fe and Mo used to compute pyrometric temperatures

	Fe	Mo
445 nm	2.39 + 3.23i	3.18 + 3.37i
747 nm	3.49 + 4.18i	3.80 + 4.25i

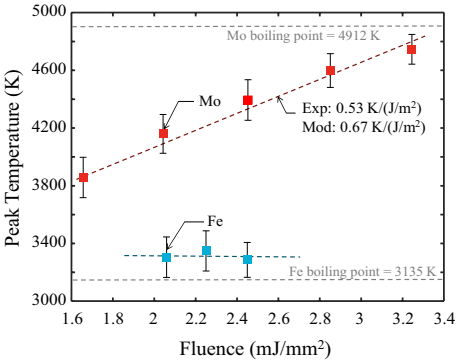

Fig. 9 Peak pyrometric temperatures measured from the Fe and Mo aerosols as a function of laser fluence. Both Fe and Mo peak temperatures are regressed with the best fit linear curves (dashed curves). The slope for Mo is compared to the value computed from Eq. (14) with a simulated aggregate structure consisting of 40 primary particles, each with a diameter of 33 nm, and fractal parameters, $k_f = 1.3$ and $D_f = 1.78$

stated, all pyrometric temperatures are computed with Eq. (9) using refractive indices obtained from Ref. [40] for Fe and Ref. [41] for Mo at 3000 K (cf. Table 1), with the understanding that the pyrometric temperature is an approximation of the true temperature due to polydispersity as discussed previously.

Signals from the Fe aerosol are weaker and noisier due to low concentrations from the SDG and smaller aggregates sizes compared to Mo. The Mo aerosol reaches higher peak temperatures.

4.2 Variation of peak pyrometric temperatures with laser fluence

Figure 9 shows how the peak pyrometric temperatures measured from the Fe and Mo aerosols vary with laser fluence. Intuitively, one would expect that higher temperatures are reached by nanoparticles with larger absorption cross-sections. For the same particle morphology, according to Mie theory, Fe nanoparticles will absorb more 1064 nm radiation compared to Mo nanoparticles. However, because Fe has a larger thermal mass (the coefficient of dT/dt in Eq. (1)) than Mo for a given spectral absorption cross-section, the Mo nanoparticles reach higher temperatures for the same laser fluence.

The peak pyrometric temperatures for the Mo aerosols are higher than the melting point of bulk molybdenum (2869 K) and greatly exceed the peak temperatures reported by Sipkens et al. [9] (see also Fig. 1b) at similar fluences and nanoparticle sizes. The peak temperatures for the Mo aerosol in this study increase approximately linearly with fluence while those of the Fe aerosols remain constant at a temperature slightly above the boiling temperature of iron at atmospheric pressure, 3135 K. Due to its low melting point, any increase in the laser energy absorbed by the Fe nanoparticles is offset by increased evaporative cooling. A slight superheating effect would be expected due to the fact that the temporal width of the laser pulse is shorter than the characteristic time of evaporation [29].

It is notable that Gurentsov et al. [21] reported a similar plateau behavior for their measurements on a Mo aerosol at ~ 4000 K, although their measurements were carried out at somewhat higher fluences (up to 6 mJ/mm^2) compared to those in this study.

In the case of Mo nanoparticles, the peak temperature should increase linearly with fluence if the evaporative cooling in Eq. (1) is negligible. Equating the increase in sensible energy to the laser heating term results in

$$\frac{dT_{peak}}{dF_0} = \frac{3}{2}\frac{Q_{\lambda.abs}d_v^2}{d_p^3 N_p \rho_m c_p} \tag{14}$$

where d_v is the volumetric equivalent diameter of the nanoaggregate, $Q_{\lambda,abs}$ is the volumetric absorption efficiency of the aggregate, and all other terms are as defined in Eqs. (1) and (4). With a simulated aggregate structure consisting of 40 primary particles, each with a diameter of 33 nm, and fractal parameters, $k_f = 1.3$ and $D_f = 1.78$, the slope of the peak temperature as a function of fluence is 0.67 K/(J/m^2) which is in close agreement with the experimental value of 0.53 K/(J/m^2) within modeling error that may originate from the uncertainty of the aggregate structure. At higher fluences, a plateau in the peak pyrometric temperatures is expected in the vicinity of the boiling point of Mo similar to that observed for Fe due to an increasing contribution of evaporation heat loss with increasing fluence.

It is worth noting, however, that the melting and boiling points of the nanoparticles are approximated to be that of the bulk. Although, literature has shown that such properties vary inversely with $1/d_p$ due to the Kelvin effect [42, 43], it is negligible for the size classes of nanoparticles considered in this work.

4.3 Enhanced absorption due to aggregate structure

LII measurements on metal nanoparticles are often interpreted as originating from isolated spheres without

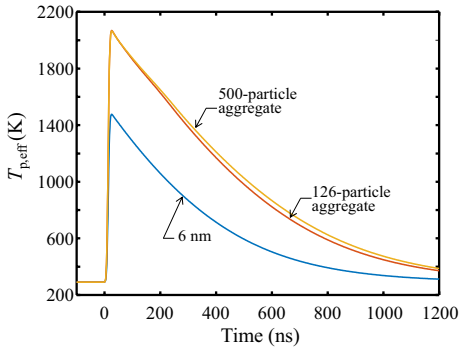

Fig. 10 Simulated pyrometric temperature curves for Fe nanoaerosol with a morphology consisting of one isolated 6-nm-diameter primary particle, and two aggregates of 126 and 500 primary particles

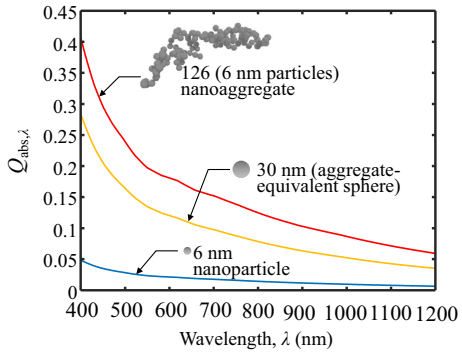

Fig. 11 Absorption enhancement of a 6-nm-diameter Fe nanoparticle by an aggregate consisting of 126 primary particles having diameters of 6 nm and $k_f = 1.3$ and $D_f = 1.78$, normalized by the geometric cross-section of a volume equivalent sphere. The spectral absorption efficiency of the volume equivalent sphere of the aggregate is plotted for comparison. The spectral absorption efficiency of a Fe aggregate is computed with MSTM, while those of the spheres are found using Mie theory

considering aggregation [9, 10, 44]. Following this assumption, the simulated temperature evolution of a 6 nm Fe nanoparticle aerosolized in N_2 and irradiated with a fluence of 2.45 mJ/mm^2 results in a peak pyrometric temperature of about 1477 K, as seen in Fig. 10. However, Fig. 11 shows that aggregates have a significantly larger absorption cross-section and that the aggregate structure also enhances the absorption cross-section when compared to a volumetric equivalent sphere due to the dipole–dipole coupling between the small primary sphere that enhances the exciting field [45]. (Simulated aggregates are generated using the cluster–cluster aggregation (CCA) algorithm [24]). Assuming an aggregate structure consisting of 126 primary particles, each having a diameter of 6 nm, as per the analysis of the TEM micrographs, and with $k_f = 1.3$ and $D_f = 1.78$, the enhanced absorption cross-section results in a peak pyrometric temperature of 2068 K. As an extreme scenario, the model assumes that each aggregate maintains its structure throughout the heating process and does not sinter into a sphere, which would reduce the absorption cross-section.

Using Eq. (13) with a viscosity of 10.5 mPa·s [46], surface tension of 1.8 J/m^2 [47], and an aggregate morphology of 126 × 6 nm diameter particle with a $D_f = 1.78$, the characteristic sintering time of the aggregate is estimated to be ~ 0.04 ns, suggesting that the aggregates sinter into spheres well before the end of the laser pulse (~ 8 ns).

To examine how sintering may impact the peak pyrometric temperature, the incandescence signal from monodisperse aerosols containing particles of different diameters is modeled with Eqs. (1) and (5), and peak pyrometric temperature is then calculated using Eq. (9). Figure 12a shows that the peak temperature increases as a function of equivalent diameter to a maximum of 2356 K at 255 nm, and then decreases with further increase in diameter. This decrease is due to a large thermal mass of the larger particles that are large enough to counteract the increase in the absorption cross-section in the energy balance equation.

Figure 12b examines how the polydispersity of particle sizes may affect the pyrometric temperature, by considering the peak pyrometric temperatures of aerosols containing particles having different lognormally

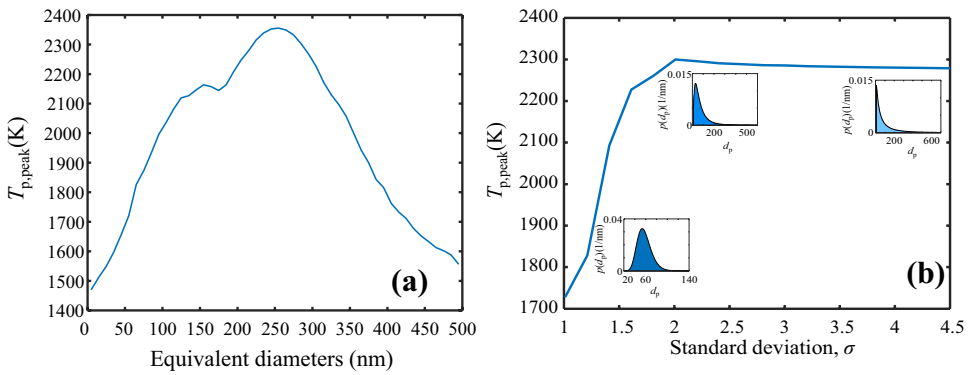

Fig. 12 Modeled peak temperatures for: **a** an aerosol of monodisperse aerosol of iron spheres as a function of particle size; **b** polydisperse aerosols composed of iron spheres, each having diameters that obey lognormal distributions sharing the same mean but different widths

distributed diameters, but with the same mean diameter of 57 nm. The peak temperatures of the aerosol increase with an increase in the standard deviation. This is because the largest particles have a larger influence on the incandescence signal, both due to their larger absorption cross-section and the fact that they reach a higher peak temperature.

Since Fe nanoparticles readily oxidize when exposed to air [48] and form a thin oxide shell, we also considered the possibility of absorption enhancement by an iron core–oxide shell structure. However, results based on absorption efficiencies computed from Mie theory for a thin shell thickness of 1–2 nm show only a slight peak pyrometric temperature increase of ~ 100 K for a range of iron cores between 70 and 270 nm.

It is worth noting that, in the case of LII measurements on aerosols of Fe nanoaggregates, the LII signal and pyrometric temperature may be modeled reliably using Mie theory since the particles are all likely to be spherical due to rapid viscous sintering. Furthermore, for reasonably small metal nanoparticles, it can be shown that $C_{abs,\lambda}{}^{Mie} = C \cdot C_{abs,\lambda}{}^{Rayleigh}$, where C is a constant that is approximately independent of wavelength [49]. Therefore, parameters like the thermal accommodation coefficient that were inferred from LII measurements on Fe aerosols assuming the Rayleigh model may be representative of the thermodynamic temperature, even though the Rayleigh model may under-predict the absorption cross-section of the particles significantly or sintered spheres grow in diameter and conduct heat in the transition or continuum regime.

4.4 Anomalous cooling from grain boundary sintering

The anomalous cooling effect is apparent from the rapid decay in pyrometric temperature observed in Fig. 8b after the peak temperature. It is more apparent in Fig. 13, which shows the logarithm of the difference between particle temperature and gas temperature versus time. In the absence of evaporative cooling, this temperature difference represents the "driving potential" for conduction, and, in conduction-dominated cooling, one would expect the temperature to decay roughly exponentially, or linearly on a semi-log plot [50]. Instead, Fig. 13 reveals a period of enhanced temperature decay that lasts approximately for 400 ns. This timescale was found to increase with increasing fluence. The difference between the experimental and expected value of ln(Tp,eff− Tg) has been labeled, Δlnθp,eff. Heat transfer calculations exclude the possibility that this super-exponential temperature decay is due to evaporative cooling (see Supplemental Information.)

We consider several alternate hypotheses to explain this phenomenon. First, it has been speculated in the literature that enhanced absorption and anomalous cooling may be due to contamination of the LII signal by neutral Bremsstrahlung emission from a plasma enveloping the nanoparticle. Talebi-Moghaddam et al. [17] show that inverse neutral Bremsstrahlung emissions are gas dependent due to the electron momentum cross-section increasing with an increase in polarizability; hence, more polarizable gas molecules should produce more Bremsstrahlung emissions from the aerosol. On the contrary, Fig. 14a demonstrates that the pyrometric peak temperature is independent of the bath gas, while Fig. 14b shows that pyrometric temperatures have the same initial temperature decay regardless of the bath gas. This discounts the possibility that the anomalous cooling phenomenon is due to neutral Bremsstrahlung. Furthermore, Bremsstrahlung radiation is also due to the scattering of the thermionically emitted electrons from the ionized nanoparticle evaporated species; however, the amount of bath gas molecules exceeds that of evaporative species; hence, the resulting radiation is significantly less than Bremsstrahlung from the bath gas [17]. These findings are consistent with the theoretical calculations from Talebi-Moghaddam et al. [17] that no Bremsstrahlung emissions are expected at laser fluences below 10 mJ/mm^2.

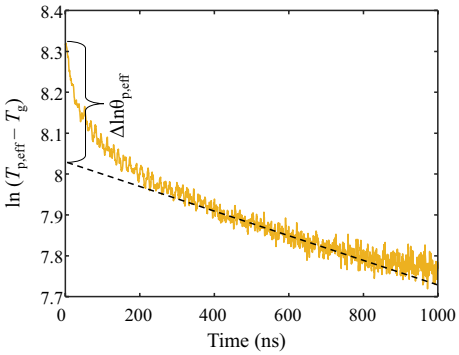

Fig. 13 Pyrometric temperatures of Mo aerosol as a function of time, showing the duration of the anomalous cooling. The gas temperature is taken as 293 K and the peak temperature of the Mo aerosol is 2395 K

Figure 15 shows the contribution of the evaporative and conductive cooling terms to the temperature history of an Fe and Mo nanoaerosol. Figure 15b shows that even at such high temperatures, in the case of Mo–Ar, conduction dominates the nanoparticle cooling for most of the cooling times, while in the case of Fe–N_2 (cf. Fig. 15a), evaporation is the dominant mode of cooling for the first ~ 400 ns.

Since the pyrometric temperatures of the Mo nanoaerosol reach temperatures above the melting point of molybdenum, one would expect Mo nanoaggregates to sinter through the viscous mechanism over a timescale similar to those predicted for the Fe nanoparticles. This observation is supported by the TEM images shown in Fig. 7b.

Nevertheless, we explore the possibility that the observed pyrometric temperature decay may not be indicative of the true thermodynamic temperature of the particles, but rather a spectroscopic phenomenon caused by laser-induced morphological changes to the particle that occur over a similar timescale, i.e., grain boundary diffusion. This exploration is grounded in the possibility that the true temperature of some aggregate size classes may not reach the observed pyrometric temperature (Fig. 2) but remain at temperatures that favor grain boundary sintering. Since the absorption cross-sections of aggregates are much larger than spheres of equivalent volume (Fig. 11), these unmelted aggregates would increasingly influence the pyrometric temperature as the particles cool.

The potential effect of such a scenario on the pyrometric temperature is illustrated by comparing the spectral absorption efficiencies of ten randomly oriented aggregates with those of a fully sintered sphere after the laser pulse.

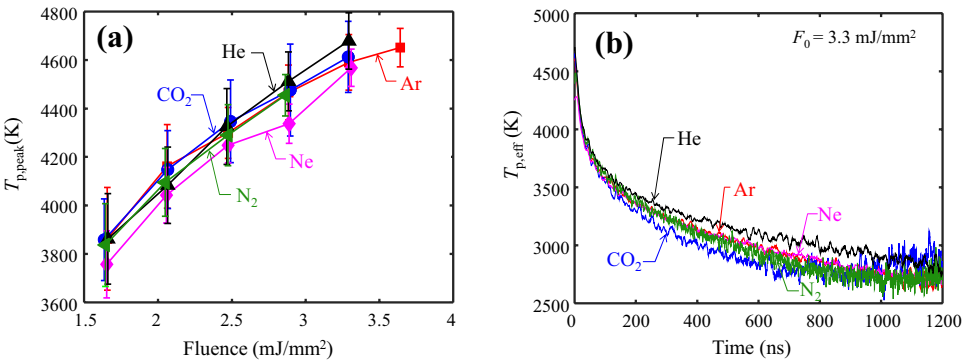

Fig. 14 Pyrometric temperatures from aerosols of Mo nanoparticles in various motive gasses

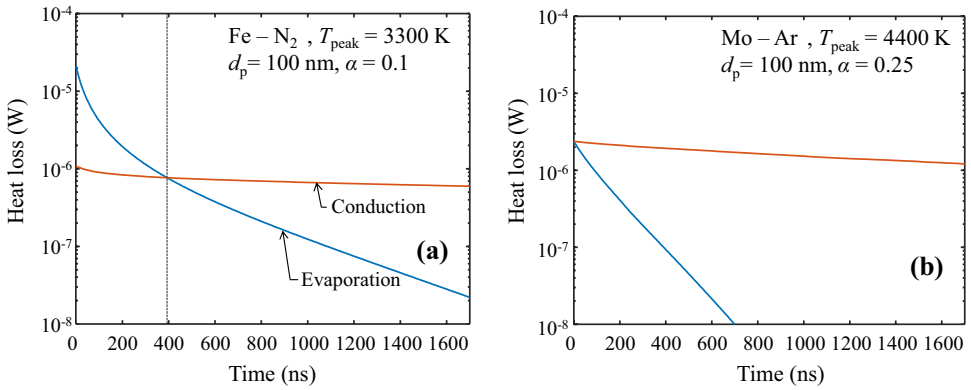

Fig. 15 Temporal comparison of heat loss terms for **a** Fe-N2 and **b** Mo-Ar nanoaerosols.Plots are generated by computing the evaporative and conductive cooling terms for an aggregatewith an equivalent volumetric diameter of 100 nm. The thermal accommodation of Fe-N_2 andMo-Ar are taken as 0.1 and 0.25 respectively, consistent with Ref. [9]. The initial temperaturesfrom which the Fe and Mo nanoparticles cool are taken as 3300 K and 4400 K, respectively, asinformed by the peak temperatures in Fig. 9. The mid-fluence temperature of Mo is consideredto be a representative value for the fluence ranges considered

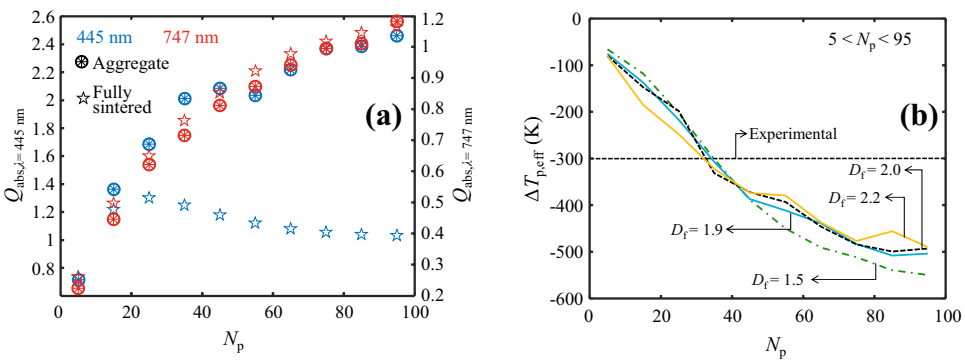

Fig. 16 **a** Changes in absorption efficiency between Mo aggregates of various sizes and a fully sintered sphere having the same *dv* at a wavelength of 445 nm and 747 nm; **b** corresponding difference between peak pyrometric temperatures and expected peak temperatures as a function of *Df* and *Np*

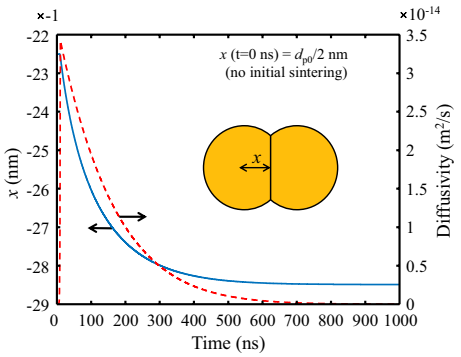

Fig. 17 Evolution of grain boundary distance between two Mo nanoparticles and the diffusivity at the grain boundary

Figure 16a shows that the spectral absorption efficiency at the lower detection wavelength (445 nm) drops significantly due to sintering, while the spectral absorption efficiency at the higher detection wavelength (747 nm) remains mostly unchanged. Therefore, the ratio of $Q_{abs,\lambda 1}/Q_{abs,\lambda 2}$ in Eq. (7) will drop during and after laser heating, leading to an apparent drop in temperature, $\Delta T_{p,eff}$, as shown in log-space in Fig. 16b, which also shows that the magnitude of the drop increases for larger aggregates. The variation in pyrometric temperature is consistent with what is observed experimentally over the anomalous cooling period.

Equations (11) and (12) are evaluated to determine the timescale of an assumed grain boundary sintering of Mo nanoaggregates. The temperature history of the nanoparticles is obtained from the simulated temperature of a 45 nm Mo nanoparticle irradiated with a fluence of 2 mJ/mm^2 and reaches a peak temperature of 2380 K. Note that radiation is still negligible compared to evaporation and conduction at the high experimental temperatures of about 4000 K. The nanoparticles are assumed to still be in point contact at the peak temperature at which point they begin to sinter.

From Fig. 17, the grain boundary distance and diffusivity reach steady-state between 400 and 500 ns which suggests that morphology changes continue to occur for a few hundreds of nanoseconds following the peak temperature. The time scale of evaluated grain boundary sintering is consistent with the time scale of anomalous cooling, further suggesting that sustained morphology changes after the laser pulse could be contributing to the apparent rapid drop in temperature. However, further investigation still needs to be carried out to ascertain the exact time scale of sintering for the Mo nanoaggregates and how this may affect the observed pyrometric temperature.

5 Conclusion

TiRe-LII is a promising technique for characterizing metal nanoaerosols, although the phenomena of excessive absorption and anomalous cooling, commonly observed features in LII measurements on metal aerosols, must be understood in order for this technique to be considered reliable for these types of nanoparticles. Several hypotheses have been advanced to explain these phenomena, including the possibility of signal corruption due to Bremsstrahlung emission from a plasma. However, this study suggests a simpler explanation: the spectroscopic model used in the majority of LII studies on metal aerosols assumes that the particles exist as isolated nanospheres, which is often not the case.

From the analysis of Fe nanoaerosols, it was found that although aggregation enhances the absorption cross-sections of the nanoparticles, simulated peak pyrometric temperatures still do not reach experimentally observed pyrometric temperatures. Irradiated TEM samples showed that the Fe aggregates rapidly sintered through viscous forces during laser heating and calculated viscous sintering times indicated full sintering to occur before the peak temperature is reached, hence suggesting that observed emissions may come from large, sintered spheres.

Although the pyrometric temperatures of the Mo aerosols suggested viscous sintering may occur, the duration of the anomalous cooling phenomena is consistent with the timescales required for grain sintering. Moreover, the change in absorption cross-section as the particles sinter would manifest as a drop in temperature. We speculate that some of the aggregates do not reach the melting point of Mo, and these aggregates dominate the LII signal due to their much larger absorption cross-section compared to fully sintered spheres.

Further investigations are needed to fully explore other effects related to aggregation such as overlapping primary particles and orientation-specific absorption cross-sections. In addition, refractory metals with higher melting and boiling points, such as tungsten, could be examined with the LII technique to explore whether the anomalous cooling phenomenon occurs for these materials and whether the duration is consistent with the diffusion coefficients.

The simulated aggregates in this work consist of primary particles in point contact; however, some overlap between primary particles may be present, which could locally intensify the electromagnetic field during laser heating of the aggregate through an “antenna effect”, thereby further enhancing the absorption cross-section [51]. This scenario could be investigated using more computationally expensive methods such as the discrete-dipole approximation [52].

Supplementary Information The online version contains supplementary material available at https://doi.org/10.1007/s00340-022-07964-y.

Acknowledgements The authors are grateful to the National Research Council (NRC) for their technical support, Prof. Steve Rogak for providing the spark discharge generator and Dr. Tim Sipkens for helpful discussions.

Author contributions SR-E: conceptualization, investigation, methodology, validation, software, formal analysis, writing—original draft, writing—review and editing. ST-M: conceptualization, investigation, methodology, software, formal analysis, writing—review and editing. KJD: conceptualization, writing—review and editing, supervision, funding acquisition.

Funding This research was supported by the Natural Science and Engineering Research Council Discovery under Grant No. RGPIN-2018-03756. Stephen Robinson-Enebeli acknowledges funding from the Indigenous and Black Engineering Fellowship (IBET).

Data availability The datasets generated during and/or analyzed during the current study are available from the corresponding author on reasonable request.

Declarations

Conflict of interest The authors declare that they have no known competing financial interests or personal relationships that could have appeared to influence the work reported in this paper.

References

1. X. Guo, Z. Yang, H. Dong, X. Guan, Q. Ren, X. Lv, X. Jin, Simple combination of oxidants with zero-valent-iron (ZVI) achieved very rapid and highly efficient removal of heavy metals from water. Water Res. **88**, 671–680 (2016)
2. K. Jiang, D.A. Smith, A. Pinchuk, Size-dependent photothermal conversion efficiencies of plasmonically heated gold nanoparticles. J. Phys. Chem. C **117**(51), 27073–27080 (2013)
3. J. Beik, Z. Abed, F.S. Ghoreishi, S. Hosseini-Nami, S. Mehrzadi, A. Shakeri-Zadeh, S.K. Kamrava, Nanotechnology in hyperthermia cancer therapy: from fundamental principles to advanced applications. J. Control. Release **235**, 205–221 (2016)
4. L. Wang, M. Zheng, Z. Xie, Nanoscale metal-organic frameworks for drug delivery: a conventional platform with new promise. J. Mater. Chem. B **6**(5), 707–717 (2018)
5. A. Boiarciuc, F. Foucher, C. Mounaïm-Rousselle, Soot volume fractions and primary particle size estimate by means of the simultaneous two-color-time-resolved and 2D laser-induced incandescence. Appl. Phys. B **83**(3), 413 (2006)
6. R. Lemaire, M. Mobtil, Modeling laser-induced incandescence of soot: a new approach based on the use of inverse techniques. Appl. Phys. B Lasers Opt. **119**(4), 577–606 (2015)
7. H.A. Michelsen, C. Schulz, G.J. Smallwood, S. Will, Laser-induced incandescence: particulate diagnostics for combustion, atmospheric, and industrial applications. Prog. Energy Combust. Sci. **51**, 2–48 (2015)
8. S. Robinson-Enebeli, S. Talebi-Moghaddam, K.J. Daun, Time-resolved laser-induced incandescence measurements on aerosolized nickel nanoparticles. J. Phys. Chem. A **125**(28), 6273–6285 (2021)
9. T.A. Sipkens, N.R. Singh, K.J. Daun, Time-resolved laser-induced incandescence characterization of metal nanoparticles. Appl. Phys. B Lasers Opt. **123**(14), (2017)
10. B.F. Kock, C. Kayan, J. Knipping, H.R. Orthner, P. Roth, Comparison of LII and TEM sizing during synthesis of iron particle chains. Proc. Combust. Inst. **30**(1), 1689–1697 (2005)
11. A. Eremin, E. Gurentsov, C. Schulz, Influence of the bath gas on the condensation of supersaturated iron atom vapour at room temperature. J. Phys. D. Appl. Phys. **41**(5), (2008)
12. T.A. Sipkens, N.R. Singh, K.J. Daun, N. Bizmark, M. Ioannidis, Examination of the thermal accommodation coefficient used in the sizing of iron nanoparticles by time-resolved laser-induced incandescence. Appl. Phys. B Lasers Opt. **119**(4), 561–575 (2015)
13. T.A. Sipkens, P.J. Hadwin, S.J. Grauer, K.J. Daun, Predicting the heat of vaporization of iron at high temperatures using time-resolved laser-induced incandescence and bayesian model selection. J. Appl. Phys. **123**(9), 095103 (2018)
14. A. Eremin, E. Gurentsov, E. Popova, K. Priemchenko, Size dependence of complex refractive index function of growing nanoparticles. Appl. Phys. B Lasers Opt. **104**(2), 285–295 (2011)
15. M. Stephens, N. Turner, J. Sandberg, Particle identification by laser-induced incandescence in a solid-state laser cavity. Appl. Opt. **42**(19), 3726 (2003)
16. S. Talebi-Moghaddam, S. Robinson-Enebeli, S. Musikhin, D.J. Clavel, J.C. Corbin, A. Klinkova, G.J. Smallwood, K.J. Daun, Multiphoton induced photoluminescence during time-resolved laser-induced incandescence experiments on silver and gold nanoparticles. J. Appl. Phys. **129**(18), 183107 (2021)
17. S. Talebi Moghaddam, K.J. Daun, Plasma emission during time-resolved laser-induced incandescence measurements of aerosolized metal nanoparticles. Appl. Phys. B Lasers Opt. **124**(159), (2018)
18. S. Talebi-Moghaddam, T.A. Sipkens, K.J. Daun, Laser-induced incandescence on metal nanoparticles: validity of the Rayleigh approximation. Appl. Phys. B Lasers Opt. **125**(11), 1–16 (2019)
19. D.R. Snelling, K.A. Thomson, F. Liu, G.J. Smallwood, F. Liu, Comparison of LII derived soot temperature measurements with LII model predictions for soot in a laminar diffusion flame. Appl. Phys. B. **96**, 657–669 (2009)
20. K.J. Daun, G.J. Smallwood, F. Liu, Investigation of thermal accommodation coefficients in time-resolved laser-induced incandescence. J. Heat Transfer **130**(12), 1–9 (2008)
21. A.V. Gurentsov, E.V. Eremin, Sizing of Mo nanoparticles synthesised by Kr – F laser pulse photo-dissociation of Mo(CO)6. Appl. Phys. A Mater. Sci. Process **119**, 615–622 (2015)
22. I. Altman, Comment on 'multiphoton induced photoluminescence during time-resolved laser-induced incandescence experiments on silver and gold nanoparticles.' J. Appl. Phys **130**, 46101 (2021)
23. C.M. Sorensen, Light scattering by fractal aggregates: a review. Aerosol Sci. Technol. **35**(2), 648–687 (2001)
24. A.V. Filippov, M. Zurita, D.E. Rosner, Fractal-like aggregates: relation between morphology and physical properties. J. Colloid Interface Sci. **229**(1), 261–273 (2000)
25. F. Liu, M. Yang, F.A. Hill, D.R. Snelling, G.J. Smallwood, Influence of polydisperse distributions of both primary particle and aggregate size on soot temperature in low-fluence LII. Appl. Phys. B Lasers Opt. **83**(3), 383–395 (2006)
26. F. Liu, G.J. Smallwood, Effect of aggregation on the absorption cross-section of fractal soot aggregates and its impact on LII modelling. J. Quant. Spectrosc. Radiat. Transf. **111**(2), 302–308 (2010)
27. K.M. Watson, Thermodynamics of the liquid state. Ind. Eng. Chem. **35**(4), 398–409 (1943)
28. T.A. Sipkens, J. Menser, R. Mansmann, C. Schulz, K.J. Daun, Investigating temporal variation in the apparent volume fraction

measured by time-resolved laser-induced incandescence. Appl. Phys. B Lasers Opt. **125**(8), 1–20 (2019)
29. J. Menser, K. Daun, T. Dreier, C. Schulz, Laser-induced incandescence from laser-heated silicon nanoparticles. Appl. Phys. B **122**, (2016)
30. C.F. Bohren, D.R. Huffman, *Absorption and scattering of light by small particles* (John Wiley & Sons Inc, Canada, 1998)
31. C.M. Sorensen, J.B. Maughan, H. Moosmüller, Spherical particle absorption over a broad range of imaginary refractive index. J. Quant. Spectrosc. Radiat. Transf. **226**, 81–86 (2019)
32. M.N. Rahaman, *Sintering of ceramics* (CRC Press, 2007)
33. M.L. Eggersdorfer, D. Kadau, H.J. Herrmann, S.E. Pratsinis, Aggregate morphology evolution by sintering: number and diameter of primary particles. J. Aerosol Sci. **46**, 7–19 (2012)
34. M.L. Eggersdorfer, D. Kadau, H.J. Herrmann, S.E. Pratsinis, Multiparticle sintering dynamics: from fractal-like aggregates to compact structures. Am. Chem. Soc. **27**, 6358–6367 (2011)
35. M.L. Eggersdorfer, S.E. Pratsinis, Agglomerates and aggregates of nanoparticles made in the gas phase. Adv. Powder Technol. **25**(1), 71–90 (2014)
36. R. Mansmann, T.A. Sipkens, J. Menser, K.J. Daun, T. Dreier, C. Schulz, Detector calibration and measurement issues in multi-color time-resolved laser-induced incandescence. Appl. Phys. B **125**(7), 126 (2019)
37. N.S. Tabrizi, M. Ullmann, V.A. Vons, U. Lafont, A. Schmidt-Ott, Generation of nanoparticles by spark discharge". J. Nanoparticle Res. **11**(2), 315–332 (2008)
38. Rasband, WS.: "Image J," U. S. Natl. Institutes Heal. Bethesda, Maryland, USA 1997–2018. https://imagej.nih.gov/ij/.
39. R.J. Samson, G.W. Mulholland, J.W. Gentry, Structural analysis of soot agglomerates. Langmuir **3**, 272–281 (1987)
40. S. Krishnan, K.J. Yugawa, P.C. Nordine, Optical properties of liquid nickel and iron. Phys. Rev. B **55**(13), 8201–8206 (1997)
41. B.T. Barnes, Optical constants of incandescent refractory metals. J. Opt. Soc. Am. **56**(11), 1546 (1966)
42. T.H. Wang, Y.F. Zhu, Q. Jiang, Size effect on evaporation temperature of nanocrystals. Mater. Chem. Phys. **111**(2–3), 293–295 (2008)
43. K.K. Nanda, Bulk cohesive energy and surface tension from the size-dependent evaporation study of nanoparticles. Appl. Phys. Lett. **87**(2), 021909-1-021909–3 (2005)
44. E.V. Gurentsov, A.V. Eremin, Size measurement of carbon and iron nanoparticles by laser induced incadescence. High Temp. **49**(5), 667–673 (2011)
45. G.W. Mulholland, C.F. Bohren, K.A. Fuller, Light scattering by agglomerates: coupled electric and magnetic dipole method. Langmuir **10**, 2533–2546 (1994)
46. Y. Deng, J. Zhang, K. Jiao, Viscosity measurement and prediction model of molten iron. Ironmak. Steelmak. **45**(8), 773–777 (2018)
47. S. Schönecker, X. Li, B. Johansson, S.K. Kwon, L. Vitos, "Thermal surface free energy and stress of iron." Sci. Rep. **5**(1), 1–7 (2015)
48. C. Wang, D.R. Baer, J.E. Amonette, M.H. Engelhard, J. Antony, Y. Qiang, Morphology and electronic structure of the oxide shell on the surface of iron nanoparticles. J. Am. Chem. Soc. **131**(25), 8824–8832 (2009)
49. H. Moosmüller, C.M. Sorensen, Small and large particle limits of single scattering albedo for homogeneous, spherical particles. J. Quant. Spectrosc. Radiat. Transf. **204**, 250–255 (2018)
50. K.J. Daun, Thermal accommodation coefficients between polyatomic gas molecules and soot in laser-induced incandescence experiments. Int. J. Heat Mass Transf. **52**(21–22), 5081–5089 (2009)
51. H. Wei, H. Xu, Hot spots in different metal nanostructures for plasmon-enhanced Raman spectroscopy. Nanoscale **5**(22), 10794–10805 (2013)
52. B.T. Draine, P.J. Flatau, Discrete-dipole approximation for scattering calculations. J. Opt. Soc. Am. A **11**(4), 1491 (1994)